ORIGINAL PAPER

Structural and microstructural features of Neoproterozoic granites in Figuil: Constraints in ductile shear deformations of the Guider Sorawel shear zone

Basua Afanga Archelaus Emmanuel[1,2] · Changqian Ma[2] · Kanouo Sylvestre Nguo[3] · Lian-Xun Wang[2] · Soumyajit Mukherjee[4] · Bovari Youmin Syprien[2] · Yu-Xiang Zhu[2] · Siggy Signe Nformidah- Ndah[5] · Robison Eben Mboe[6]

Abstract

A less prominent N-S oriented continental-scale strike-slip shear zone occurs within the Babouri-Figuil Magmatic Complex (BFMC). Studies have shown that such shallow to middle crustal levels shear zones often display long-lasting deformation, physical expression of strain localization, and mineralization. However, until dates, deformation evolution and structural mineralization of this ~ 8 km long shear zone in Babouri-Figuil remain enigmatic, which prompted its investigation. A combined structural study supported by U-Pb zircon dating on the sheared granitoids is reported. Biotite granite sampled near Sorawel village yielded zircon U-Pb concordia age of 606 ± 6 Ma, whereas hornblende-biotite granite sampled at the western corner of the Ribao massif yielded zircon U-Pb concordia age of 601 ± 2 Ma. These granites were emplaced in a transpressive tectonic regime shortly after a regional thickening event < 620 Ma. The studied microstructures demonstrate a typical transition from protomylonite to extremely deformed mylonite marked with decreased mineral sizes. On thin sections, two main zones are identified: "zone A" (low-strain zone) and "zone B" (high-strain zone). Core-mantle K-feldspar porphyroclasts within the mylonite show dislocation creep deformation, whereas recrystallized to neocrystallized aggregates indicate plastic flow by viscous grain boundary sliding. Shear sense indicators revealed both early dextral and late sinistral shearing. In all, the results revealed that the Guider-Sorawel shear zone (GSSZ) experienced ductile deformation probably under medium to high temperature conditions. The double shearing is possible during the switch of the regional maximum principal stress from N-S (~ 585 Ma) to NW-SE (< 580 Ma). The obtained dates are syn-collisional and are consistent with D2 deformation phase in other parts of Cameroon. Also, the dates marked the final tectonic college between the north Cameroon domain and the southwest Chad domain, which probably might have induced the SZ. The construction of these adjacent domains probably resulted to a sort of increased temperature and strain localization that led to the initiation of a rheologically weaken mechanical zone via which the magma generated flows to near surface crustal level.

✉ Basua Afanga Archelaus Emmanuel
  basfanga@yahoo.com

[1] Department of Geology, University of Buea, P.O. Box 63, Buea, Cameroon

[2] School of Earth Sciences, China University of Geosciences, 430074 Wuhan, People's Republic of China

[3] Mineral Exploration and Ore Genesis Unit, Department of Mining Engineering and Mineral Processing, Faculty

of Mines and Petroleum Industries, University of Maroua, Maroua, 08 Kaélé, Cameroon

[4] Department of Earth Sciences, Indian Institute of Technology Bombay, Powai, Mumbai, Maharashtra 400 076, India

[5] Institut fur Geologie, Universitat Bern, Baltzerstrasse 1 + 3, Bern, Switzerland

[6] National Hydrocarbons Corporation (SNH), Yaoundé, Cameroon

Introduction

Microstructures in rocks are features whose studies can provide significant information on the evolution of a tectonic domain in case where rocks are characterized by several tectonic deformations (Radlinski et al. 2005; Mukherjee and Koyi 2010; Mukherjee 2013; Fazio et al. 2020; Punturo et al. 2014; Nsengimana and Kumar 2019). Microstructures have been classified into three main crustal-mantle tectonomagmatic events: magmatic, sub-magmatic, and solid states (Coleman et al. 2005). Rocks possessing these states are inferred to have undergone prolong stress and temperature disturbances (Coleman et al. 2005). The solid-state features are often considered to be derived from increase stress presumably at low temperatures accompanying deformation possibly after the complete crystallization of magmas (Coleman et al. 2005; Punturo et al. 2014). Detail microstructural studies can reveal important information on the tectonic events especially in rocks lacking macroscopic signatures (Passchier and Trouw 2005; Mukherjee and Koyi 2010). Moreover, in complex systems, associating microstructures with age dating of the host rock is a good way to critically constrain the age of the associated tectonic deformations (e.g., Archanjo et al. 2008).

Cameroon found in the Central African Fold Belt is divided into at least three main geotectonic zones limited by major tectonic structures (e.g., Ngako et al. 2008). These are the southern domain (Yaounde domain), central domain (Adamawa-Yade domain), and the northwest-Cameroon domain (Fig. 1(a), (b)). Studies show that the central domain in particular displays the most tectonic features (Toteu et al. 2001; Ngako et al. 2008; Njonfang et al. 2008). It principally hosts major shear fractures that display at least three main trends. The NE-SW central Cameroon shear zone (CCSZ, SW-NE) and the Sanaga shear zone (SSZ) north and south, respectively. Moreover, these major shear zones are crosscut by minor ones such as the: Adamawa fault, Betare-Oya fault, and the Tchollire-Banyo fault that in some areas formed fan geometry (Ngako et al. 2008). According to some authors, shear movements were followed by major transpression and transtension events, respectively, (e.g., Ngako et al. 2008). Other researchers hold the opinion that pluton emplacement was an integral part of the evolution of shear zones. Several studies with controversial models have been carried out to understand the spatial and temporal relationship between regional deformation and magmatic emplacement along these shear zones (e.g., Tagne-Kamga et al. 1999; Nzenti et al. 2006; Ngako et al. 2008). In some areas, it was noted that both the sinistral and dextral shear movements seem to be synchronous (e.g., Dawaï et al. 2013), whereas in other parts, the dextral shear movement preceded the sinistral one (e.g., Ntieche et al. 2017; Efon Awoum et al.

2020). Further, techniques (e.g., an electrical method) have been applied to delineate favorable gold-bearing structures in the Betare-Oya gold district. An anomalous gold concentrates were found in N-S sinistral shear zones, faults, and fractures in southern Cameroon (Mumbfu et al. 2014). A few studies were carried out to understand the spatial-temporal relationship between gold mineralization and tectonic structures in the central Cameroon domain. The results indicate that late-plutonic activities have favored the concentration of mineral deposits such as cobalt, nickel, rutile, iron, bauxite, uranium, and gold along fractures. Although a few of the rocks that outcrop in the northwestern Cameroon domain have received such kind of studies (Ngako et al. 2008; Dawaï et al. 2013), however, no mineralization is yet to be associated with these early formed granitoids. Moreover, there is a lack of detail kinematic evolution study between the shear zones and the associated sheared granitoids in the northwest Cameroon domain. Only a few of the outcropping plutons have radiogenic dates; meanwhile, several of the plutons have merely been correlated with dated syn- to late-kinematic plutons from different tectonic zones.

In this article, we present zircon U-Pb geochronological dates from syn-collisional sheared alkaline granites and microstructural features. These results aim to (i) identify and discuss structural features to constrain and relate major tectonic events, (ii) discuss the relative time relation between plutonism and deformation, and (iii) explain the possible cause of double shear deformations in the studied SZ.

Regional geology

The Babouri-Figuil Magmatic Complex is located within the northwest Cameroon domain (Fig. 1(a), (b)). This domain is the northern segment of the Central African Orogenic Belt (CAOB). It is bordered to the east by the SW Chad domain that together represents the southern limit of the Sahara Metacraton (Shellnutt et al. 2015; Basua 2021; Basua et al. 2022). The CAOB is identified in Cameroon, Chad, and the Central Africa Republic (Penaye et al. 2006; Ngako et al. 2008; Fig. 1(a), (b)). Its formation is linked to the collision evolution between West African craton, Congo-Sao Francisco craton (Toteu et al. 2004; Van Schmus et al. 2008), and the Saharan Metacraton (Abdelsalam et al. 2002; Ngako and Njonfang 2011). The studied shear zone crosscuts the basement rocks predominantly composed of medium- to high-grade Neoproterozoic deformed gneisses and schists with the association of amphibolites and marble (Fig. 2). According to Basua (2021), the GSSZ shear zone may have played a key role in the pre- and post-magmatic processes (magma conduit and emplacement) of the associated Neoproterozoic plutons (Fig. 2). This is possible during post rejuvenation of the shear zone. The studied sheared granites indicate textural variations from augen-bearing protomylonite and mylonite
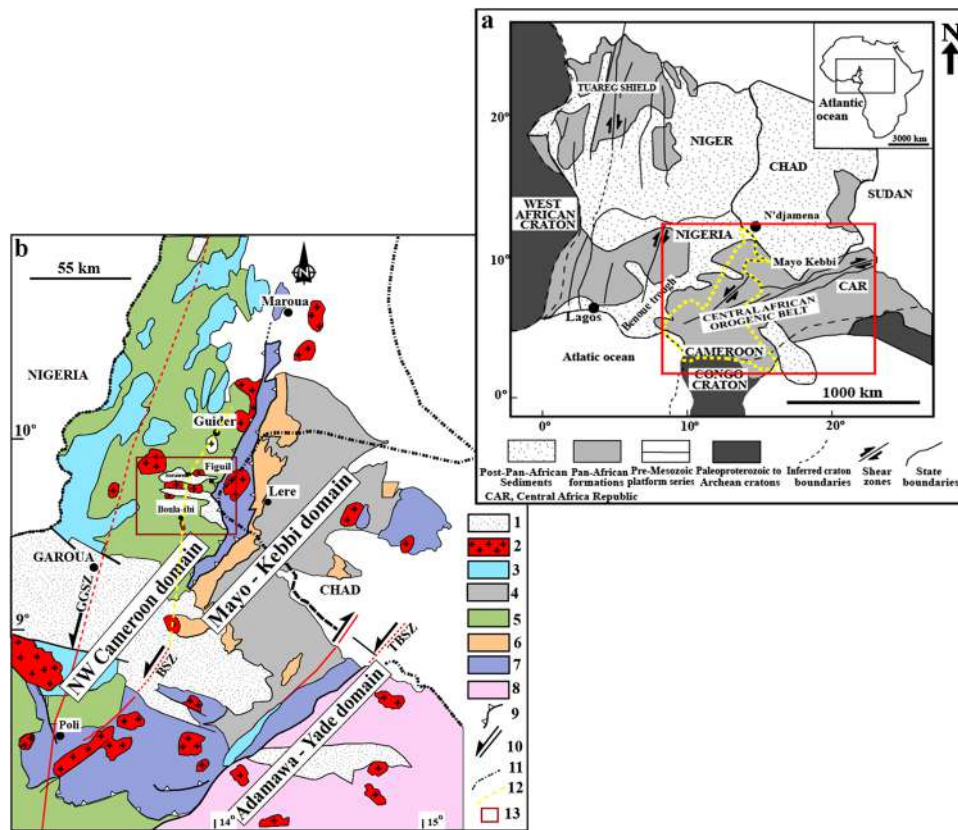
Fig. 1 (a) Map of Central and West African orogenic belts, red rectangle locating Cameroon in Central Africa. (b) Geological sketch map of northern Cameroon showing location of study area (modified after Penaye et al. 2006): (1) post-Pan-African sediments; (2) late post-tectonic Pan-African granitoids; (3) syntectonic granite; (4) Mayo Kebbi batholiths: tonalite, trondhjemite, and granodiorite; (5) medium- to high-grade gneisses of the west Cameroon domain; (6) mafic to intermediate complex of the Mayo Kebbi region (metadior-ite and gabbro-diorite) and amphibolites; (7) Neoproterozoic late- to medium-grade volcano-sedimentary sequence: Zalbi, Gouegoudoum, and Poli Groups; (8) remobilized paleoproterozoic Adamawa-Yade domain; (9) thrust front; (10) strike-slip faults, TBZ, Tchollire-Banyo shear zone, and GGSZ, Gode-Gormaya shear zone; (11) state border; (12) speculative NE extension of the Balche shear zone (BSZ); (13) red rectangle shows the location of Fig. 2 in the NCD

to ultramylonite near the shear zone and less-deformed variety having coarse to medium-grained away from the SZ (Basua 2021). It is a ductile shear zone and its trend changes from N-S in the west near the Poli town to NNE-SSW and crosscut the Godde-Gomaya shear zone (GGSZ; Ngako et al. 2008) if considered that it represents the northern extension of the Balche shear zone (BSZ). Both the GSSZ and GGZS have almost the same trends toward the north and are adjacent to each other and may have formed under the same condition and period (Fig. 1(b)).

Megascopic structural features within the shear zone

Metamorphic rock

Mylonitic banding (S_b) and mylonitic foliations (S_m) were observed in banded gneisses and schists whose protolith is presumably deformed volcanic and volcaniclastic rocks (Basua 2021; Fig. 3a–f). The S_b is marked by regular alternation of quartz-feldspar-rich and amphibole-biotite-rich layers. In some gneisses, the S_b can rich up to ~ 20–60-m thick (Fig. 3e). Sometimes, the S_b shows nearly isoclinal intrafolial folding often depicting a reclined geometry. In the gneisses and schists, lenticular feldspathic and quartzose augen are often wrapped by thin micaceous layers displaying mylonitic foliations (S_m) (Basua 2021). Only one orientation (NNE-SSW) of the mylonitic foliation (S_m) is megascopically recognizable in these rocks and is parallel with the mylonitic bedding (S_b) (Fig. 3e, f). However, under the microscope, S- and C-planes are identifiable displaying relatively small angles with each other (Basua 2021). In gneisses is commonly observed an earlier mylonitic foliations cut across by late quartzose layers. Locally, these quartzose layers show two set of planes, which are analogous to conjugate riedel shears as observed in certain banded mylonites. The earlier mylonitic foliations show sigmoidal curvatures indicating the sense of movement of the later plane. These
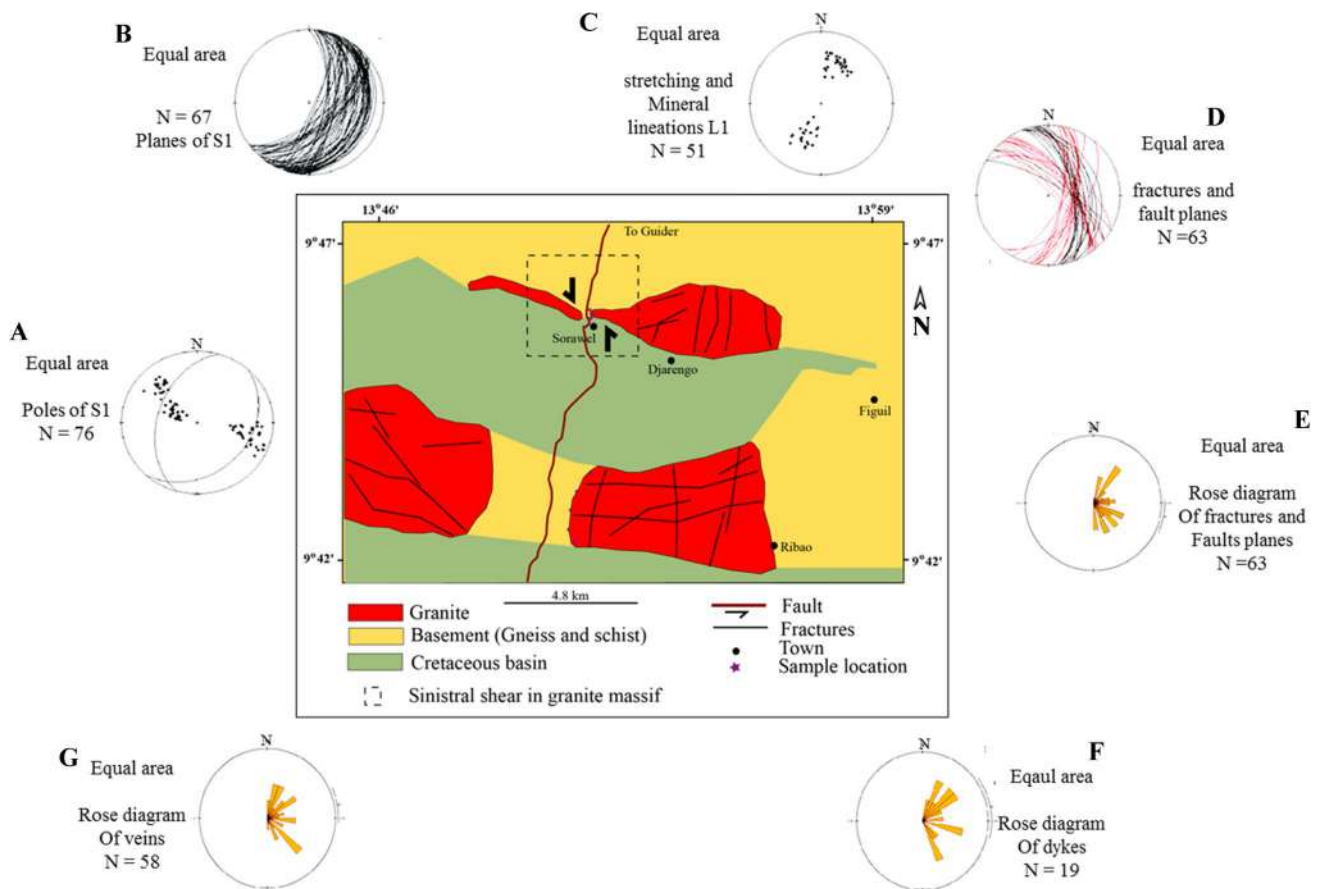
Fig. 2 Simplified geological map of the study area modified from the geologic map of Ngoundere-E of scale 1/500.000 (since 1962), showing the distribution of the alkaline granites of Figuil. Stereonets and rose diagrams are also plotted. **A** Planes of S_1 foliations in gneiss of different localities around Figuil; **B** poles of S_1 foliations; **C** stretching and mineral lineations in gneiss around Figuil; **D** fractures and fault planes in the granitic massifs of Heri, Ribao, Lombel, Badesi, and Djabe; **E** rose diagram of veins in granite massifs, **F** rose diagram of dykes with width > 2 m crosscutting basement formations; **G** rose diagram of fractures and fault planes in granitic massifs

earlier formed mylonitic foliations are also often folded into tight and intrafolial folds whose hinges form an angle with the second set of the mylonitic foliations defining vertical axial planes (Basua 2021). At places, the second set may as well be folded and cut across by later set of movement planes. The folds are associated with the mylonitic banding and have reclined geometry with axes parallel to the down-dip stretching lineation. These folds vary both in style and orientations. Some earlier folds have angular hinges, whereas the later set of folds sometimes are parallel and show nearly rounded hinges.

Granite

Pink granites are the dominant plutonic facies in the study area (Basua 2021). Weak solid-state deformation (S_1 and L_2) is observed at some pluton boundaries indicating chilled margins (Fig. 4a–c). Spotted mineral lineation trending N-S to NNE-SWW, with steep plunge resembling the lineations in the basement rock, is observed (Fig. 4a–c). In coarse-grained granite at Boula-Ibi, a minor ductile shear dextrally displaced mylonitic foliations of feldspar porphyroclasts (Fig. 4d). In another location still at Boula-Ibi, this ductile shear defined a Riedel structure (Fig. 4e, f). Ductile to brittle shear of late discrete fine-grained granitic veins of different generations is also observed locally (Fig. 5a, b). Displacement of sigmoid shape mafic xenolith in gneiss corresponds to the displacement of first-generation fault in pink granite (Fig. 5c, d). At places in the Ribao pluton, folded massifs define anticlines and synclines and indicate compression component of a regional transpression after crystallization (Fig. 5e, f). Pervasive fracturing is common in the entire outcrops and displays at most seven trends (N-S, NNE-SSW, NE-SW, E-W, ESE-WNW, SE-NW, and SSE-NNW), NE-SW being the main (Fig. 2). The diverse fractures could be related to N-S extension coeval with the formation of the two half Cretaceous grabens in the study area (Fig. 2).

Fig. 3 Field photographs showing both dextral and sinistral shear in basement rock. **a–d** Sinistral shearing crosscutting foliations (S_2) in gneisses, incline view. **e**, **f** Horizontal view of B_2 boudins of asymmetric quartzofedpathic veins in gneisses showing dextral shearing
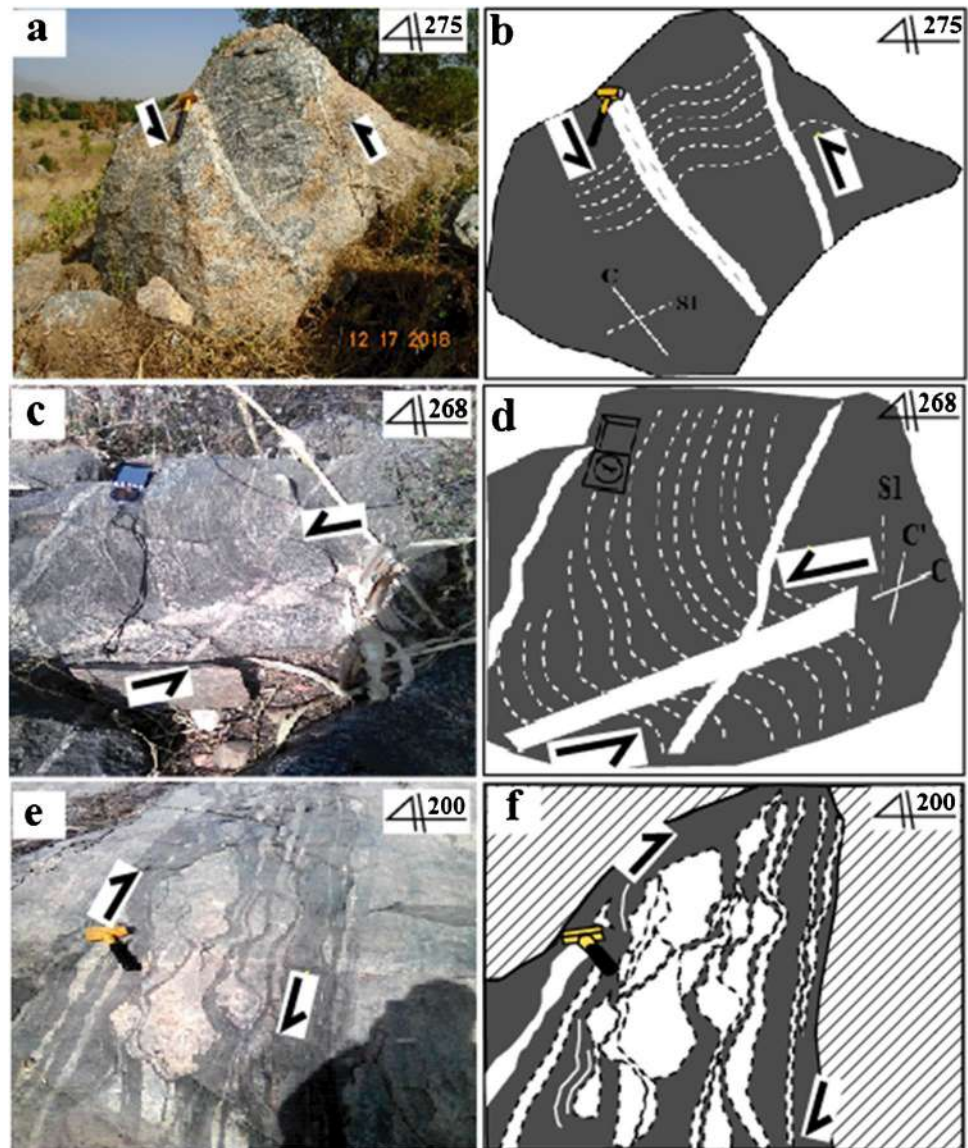

Petrography

Biotite granite on hand specimen is coarse to very coarse grained and reddish composed of red colored feldspar, quartz, and biotite. The ratio of feldspar to quartz is ~ 80:20, and grains are rarely oriented. Quartz is intergranular around feldspar laths at times associated with biotite. In thin sections, feldspars (K-feldspar, 45–50%) and plagioclase (20–25%) mainly form phenocrysts (wide, ~ 8 mm, and length, ~ 10 mm). Quartz and biotite range in proportion from 10 to 20% and 2 to 5%, respectively (Fig. 6). Some plagioclase laths enclose sericite, are zoned, and developed myrmekite at the contact with quartz and K-feldspar. Biotite flakes are found at the edge of some feldspars and quartz. Some biotite flakes have zircon inclusions, whereas others enclose green chlorite within their cleavages. Other accessory minerals found are apatite, titanite, and opaque oxides.

Hornblende-biotite granite is macroscopically medium to coarse grained and composed of feldspar, quartz, biotite, and amphibole. In thin sections, it is composed of orthoclase (20–25%), microcline (15–20%), plagioclase (20–25), quartz (15–20%), biotite (5–8%), and hornblende (2–3%). Perthites and microperthites are found in some K-feldspars. Some plagioclase laths display oscillatory zoning. Myrmekite occurs at the boundary between quartz and feldspars. Biotite flakes are locally altered to chlorite and opaque oxides. They are the main host of large zoned euhedral zircon crystals. Hornblende occurs as euhedral crystals along with biotite and opaque oxides. Accessory minerals include titanite, zircon, apatite, chlorite, spinel, and opaque oxides.

Fig. 4 Field photographs. **a–d** Horizontal view of magmatic foliations crosscut by a dextral and sinistral mylonitic shears in granite. **e**, **f** N-S oriented flanking structure (Riedel) displaying complete features in BHG at Boula-Ibi, horizontal view (Mukherjee 2014). The lengths of instruments are (1) harmer 50 cm, (2) compass 22 cm, (3) bollmaker 13 cm, (4) cap of bollmaker 3.5 cm, (5) ball pen with cap 14.1 cm, and (6) ball pen without cap 13.5 cm
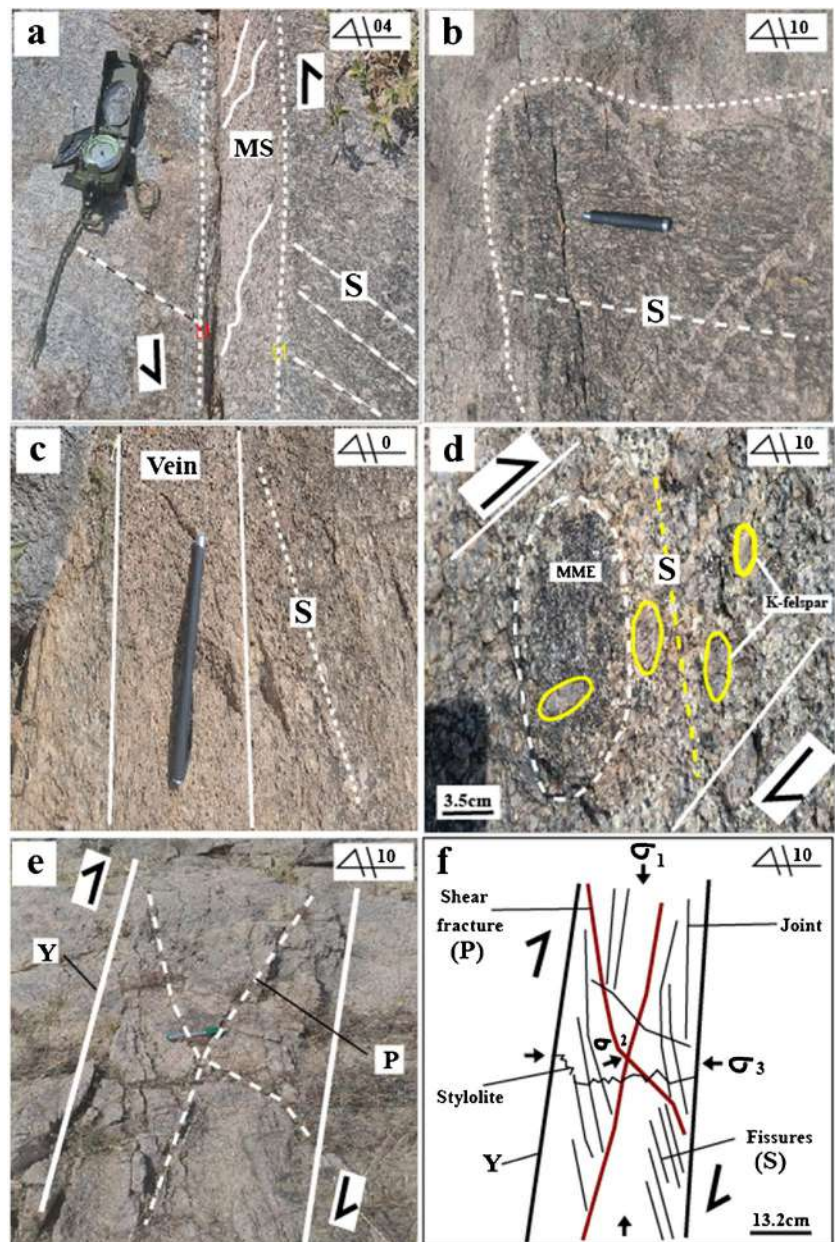

Materials and methods

Field and laboratory techniques

The studied SZ was mapped and nearby outcrops were identified and analyzed based on structural features. With the aid of a Sylva-type compass clinometer, structural measurements were performed at outcrop levels. Representative samples were collected from the sheared granitic massifs adjacent to the shear zone. The prepared thin sections were manufactured (polished down to ~ 30-μm thicknesses) and examined with the help of a petrographic microscope at the laboratories of China University of Geosciences, Wuhan. Structural data were analyzed and prepared on a stereoplot

software. Rock samples from biotite granite and hornblende-biotite granite were crushed and powdered to separate zircon crystals at the Langfang Yuneng Rock Mineral Sorting Technology Service Co., Ltd. One kilometer of rock fragments from each sample was milled. Before milling, precautions were taken to avoid any contamination. Samples were cleaned, chipped to reduce the grain size, crushed, and milled (at 1 mm grain size). Milled samples were regularly washed and panned to obtain heavy mineral concentrates, which were later dried in oven for 24 h at 50 °C. Dried concentrates were used to separate zircon crystals, which were later mounted and their cathodoluminescence (CL) images taken. Before mounting and CL imaging, zircon crystals were handpicked under a binocular microscope, mounted

Fig. 5 Field photographs showing both dextral and sinistral shear in basement rock and granite: **a**, **b** dextral and sinistral shear of granitic vein in granite, horizontal view; **c**, **d** sinistral shearing displacing mafic xenolith in gneiss and granite, respectively, horizontal view; **e**, **f** folding in granite, horizontal and incline views, respectively
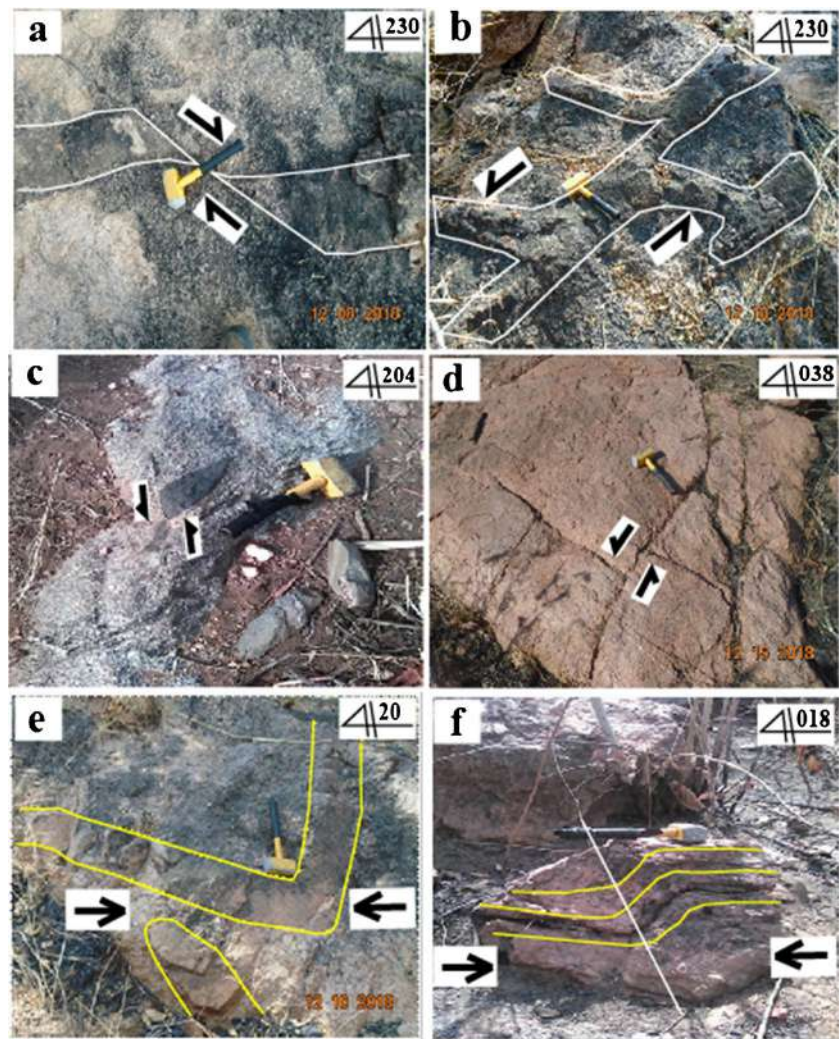

with epoxy resin on glass slide, and polished with abrasive to a standard thickens of 30 μm at the Langfang Yuneng Rock Mineral Sorting Technology Service Co., Ltd. Only selected grains of the zircon populations cathodoluminescence (CL) images were obtained using CAMECA SX51 under conditions of 50 kV and 15 nA at the Wuhan Sample Solution Analytical Technology Co., Ltd, Wuhan, China. From the obtained CL images, the internal textures for each crystal were examined. Mounted and polished zircon crystals were used for U-Pb dating.

Zircon U-Pb dating

Simultaneous U-Pb dating and zircon trace element analysis were conducted on selected mounted crystals by laser ablation–inductively coupled plasma mass spectrometry (LA-ICP-MS) at the Wuhan Sample Solution Analytical Technology Co., Ltd. These analyses were performed on an Agilent 7700e ICP-MS instrument (Agilent Technology, Tokyo, Japan) together with an excimer laser COMPexPro 102 ArF (wavelength of 193 nm and maximum energy of 200 mJ). Specific operating conditions for the laser ablation device and the ICP-MS instrument and data reduction are the same as Zong et al. (2017). In this study, a laser spot size of 32 μm was used for all analyses, with a repeating rate of 5 Hz and a fluence of 8 J/cm2. Helium was introduced as a transporter gas in the ablation cell, and argon was applied as a make-up gas behind the ablation cell (Günther and Heinrich 1999; Luo 2018) before entering the ICP via a T-connector. Also, features in this ablation system a "wire" signal smoothing and mercury remover device to obtain smooth signals and reduce the mercury signal (Hu 2014). The accuracy and precision of the analyses were enhanced by applying a small amount of (4.1 mg min^{-1}) water vapor before the ablation cell (Luo 2018). Each single-spot analysis consists of an incorporated background acquisition of ∼ 20–30 s followed by 50 s of ablation. Zircon 91500 (Wiedenbeck 1995) and glass NIST610 were considered an external standards to correct the Pb-U fractionation and
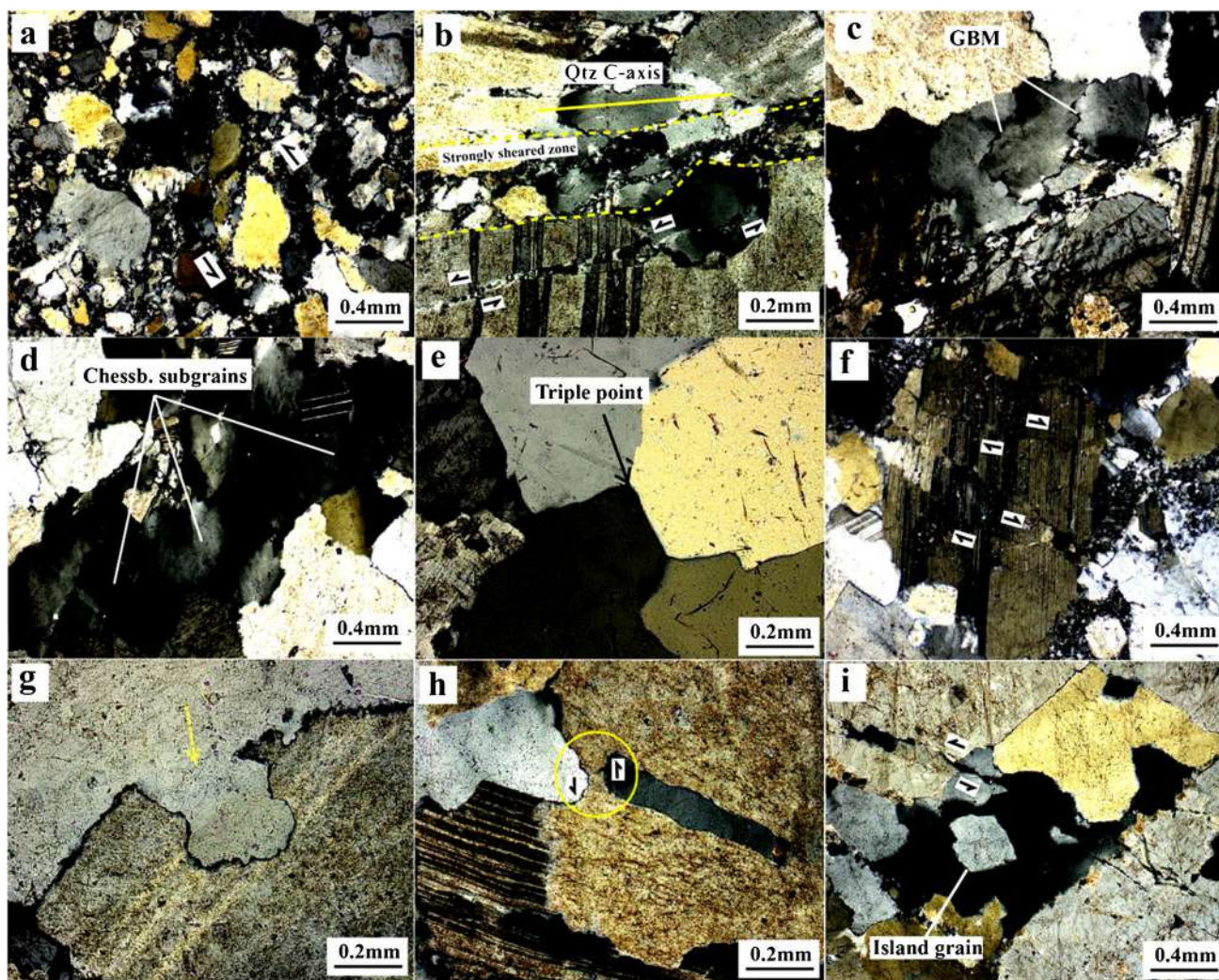
Fig. 6 Photomicrographs of granites textures under CPL: **a** lobate-oriented feldspar porphyroclasts in fine-matrix located in a sheared band, the center grain indicate sinistral shear; **b** plastic to ductile deformation in quartz along C-axis; **c** lobate contact indicating high-grade grained boundary migration (GBM) in quartz showing sweep-ing extinction; **d** chessboard subgrains in quartz; **e** quartz deformation showing triple point; **f** brittle deformation in plagioclase showing dextral dislocation; **g**, **h** lobate contact and grain boundary migration of quartz in feldspars indicating sinistral shearing after grain rotation, **i** island grains in quartz

instrumental mass discrimination, while zircon GJ-1 was analyzed as an unknown. In this study, the obtained mean ^{206}Pb/^{238}U ages of GJ-1 is 604.8 ± 4 Ma and is consistent with the reference of 599.8 ± 1.7 Ma (Jackson et al. 2004). NIST 610 and ^{29}Si were used as both external calibration and internal standardization for zircon trace element compositions, respectively (Liu et al. 2010). Excel-based program ICPMSDtaCal was used to conduct off-line selection and incorporation of background and analyte signals, time-drift correction, and quantitative calibration for trace element analysis and U-Pb dating (Liu et al. 2008; Liu et al. 2010). Concordia diagrams and measurements of the weighted mean were made using Isoplot/Ex ver3 (Ludwig 2003).

Results

Zircon CL images and U-Pb ages

Zircon CL images

The separated zircons crystals from biotite granite and hornblende-biotite granite show no particular morphological differences. They are generally euhedral and elongated (length dimension > 200 μm) prismatic to pyramidal (Fig. 7a, b). The internal structures mainly show oscillatory zoning with some twinned crystals showing core and rim variation (with brighter core and darker rim; with darker core and brighter rim). Some crystals host a darker patch in their core.

Zircon U-Pb ages

Analyzed spots in separated zircon crystals from biotite granite and hornblende-biotite granite show close to different U-Pb ages ($^{206}Pb/^{238}U$ and $^{207}Pb/^{235}U$) in Table 1 with mostly concordant plots (Fig. 8).

For zircons from biotite granite, the $^{206}Pb/^{238}U$ and $^{207}Pb/^{235}U$ ages range from 596 ± 9.5 to 608 ± 6.2 Ma and 594 ± 8.6 to 637 ± 8.5 Ma. Eight zircon grains with 95% confidences clustered on and give a concordia age of 606 ± 6 Ma with a MSWD of 1.4 and a weighted mean date of 605 ± 4 Ma (Fig. 8a, b). Sixteen zircon grains of > 95% confidence clustered between 596 and 608 Ma. These ages mainly date Ediacaran event(s).

Zircon from hornblende-biotite granite shows $^{206}Pb/^{238}U$ and $^{207}Pb/^{235}U$ ages ranging from 591 ± 4.8 to 606 ± 7.3 Ma and 588 ± 10.2 to 660 ± 8.5 Ma, which largely date Ediacaran event(s). Seven analyzed spots with low degree of discordance (< 5%) clustered on and gave a concordia age of 601 ± 2 Ma with a MSWD of 2.3 or weighted mean date of 600.9 ± 4 Ma (Fig. 8c, d).

Microstructures

The studied biotite granite and hornblende-biotite granite enclose almost similarly microstructures. Well-preserved minerals are quartz, K-feldspar, and plagioclase with small proportion of biotite, apatite, and hornblende. In most portions, these minerals are reduced into smaller fragments (Fig. 6a). Based on these, two main strain zones (zones A and B) are commonly observed. These microstructures which exhibit evidence of ductile deformation are typically of crystal reduction (Figs. 9 and 10), C-S fabrics (Fig. 10a–i); C-C′-planes (Fig. 10), microshears (Fig. 10), antithetic microfaults (Fig. 10g–i), microcracks (Fig. 10), multilayer strike-slip faults (Fig. 10i), and microveins and microboudins (Fig. 11).

Zone A (low-strain zone)

Zone A developed cataclasite to protocataclasite features. It is a low-strain zone and is marked with fragments that are a bit coarser and not necessarily bound by identified microshear bands. Here, fragments are displayed without any specific shear sense. K-feldspar is deformed to lobate shapes; crystals are randomly oriented; at times, crystals display mineral fish morphologies (Figs. 6a and 9). Quartz crystals are strongly fractured filled by late fluids sometimes composed of quartz only or a combination of quartz, biotite, and apatite. Some grains are elongated, flattened (Fig. 6b), and rotated in accordance to the shear direction. At places, some quartz grains show plastic deformation and display moderate sweeping undulose extinction (Fig. 6c), deformation bands, chessboard pattern (Fig. 6d), and interlobate boundaries. Some quartz show subhedral to anhedral grain boundaries with occasional triple points (Fig. 6e). Feldspars show brittle deformation with tapering edges close to microshear bands (Fig. 6f). Grain boundary migration is most often observed (Fig. 6g, h). Plagioclase laths developed mechanical twins and fractured locally filled by quartz. A few quartz crystals enclosed isolated crystals or island grain (Fig. 6i), with indication of recrystallization at their boundaries.

Zone B (high-strain zone)

Zone B (dominant) developed mylonites to protomylonite features, therefore a high-strain zone. Here, fragments are fined-grained and bound by defined microshear bands (Figs. 9 and 10). Mylonites to protomylonites are mostly dominated by crushed quartz and feldspar matrix enclosing a few resistant K-feldspars and quartz porphyroclasts (Fig. 10a–i). Quartz in matrix shows dynamic recrystallization indicated by serrated grain boundaries rotation and medium to high undulose extinction (Fig. 10a–d). Feldspar crystals in the matrix show lobate shapes (Fig. 10e–i).

Fig. 7 **a**, **b** Cathodoluminescence (CL) images of the representative alkaline sheared granites of Figuil. The white circles indicate analytical spots for U-Pb dating, and the yellow circles indicate analytical spots for Lu-Hf isotopes on sample HRI 40 (biotite granite) and sample RBO 23 (hornblende-biotite granite), respectively
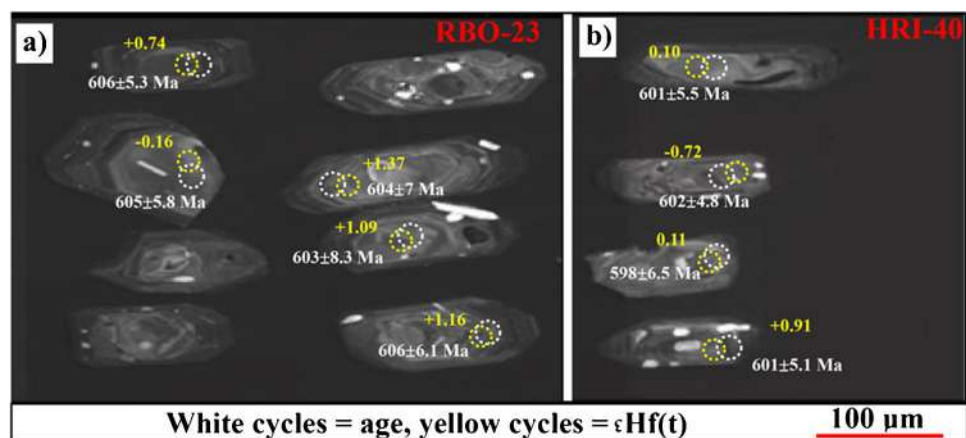
Table 1 U-Th abundance and U-Pb isotopic results for zircon crystals of sheared alkaline biotite granite and hornblende-biotite granite cropping in Figuil

Zircon spot number	Concentration (ppm)		Ratio	Isotopic ratios						Isotopic ages (Ma)					
	Th	U	Th/U	207Pb/206Pb	1σ	207Pb/235U	1σ	206Pb/238U	1σ	207Pb/206Pb	1σ	207Pb/235U	1σ	206Pb/238U	1σ
Biotite granite															
HRI40-01	4187	3589	1.2	0.0589	0.0001	0.7943	0.0151	0.0976	0.0009	561	43.5	594	8.6	600	5.3
HRI40-02	39.3	50.7	0.8	0.0574	0.0043	0.8169	0.0496	0.0977	0.0019	506	158	606	27.7	601	11.2
HRI40-03	869	1320	0.7	0.0629	0.0012	0.8563	0.0175	0.0985	0.0011	706	40.7	628	9.6	606	6.4
HRI40-04	2354	2338	1	0.0642	0.0012	0.8724	0.0156	0.0986	0.0009	746	38.9	637	8.5	606	5.3
HRI40-05	808	1272	0.6	0.0597	0.0012	0.8029	0.0156	0.0976	0.0009	594	42.6	598	8.8	600	5.4
HRI40-06	2017	2430	0.8	0.0599	0.0011	0.8162	0.0154	0.0986	0.0008	611	38.9	606	8.6	606	4.8
HRI40-07	1503	2206	0.7	0.0599	0.0001	0.814	0.0155	0.0983	0.001	611	38.9	605	8.7	605	5.8
HRI40-08	131	195	0.7	0.0615	0.0019	0.8293	0.0253	0.0982	0.0012	657	66.7	613	14	604	7
HRI40-09	186	150	1.2	0.0622	0.0021	0.8451	0.0291	0.0986	0.001	680	72.2	622	16	606	6.1
HRI40-11	50.4	63.9	0.8	0.0644	0.0045	0.8527	0.0525	0.0969	0.0016	767	142	626	28.8	596	9.5
HRI40-12	2251	3090	0.7	0.0585	0.0009	0.7957	0.0141	0.0984	0.001	550	30.6	594	8	605	5.8
HRI40-13	91.7	82.4	1.1	0.062	0.0031	0.851	0.0383	0.0975	0.0019	676	106	625	21	600	11.2
HRI40-14	1544	2030	0.8	0.0634	0.0012	0.8618	0.0155	0.0987	0.0009	720	40.7	631	8.5	607	5.3
HRI40-15	85.2	86.7	1	0.0592	0.0025	0.7938	0.0329	0.098	0.0014	572	91.5	593	18.6	603	8.3
HRI40-16	99.9	139	0.7	0.0623	0.0026	0.8376	0.0343	0.0977	0.0012	683	90.7	618	19	601	7.3
HRI40-17	1144	2127	0.5	0.0618	0.0012	0.8409	0.015	0.0989	0.0011	733	38	620	8.3	608	6.2
Biotite-hornblende granite															
RBO23-01	3105	4891	0.6	0.0594	0.0012	0.8023	0.0164	0.981	0.001	589	11	598	9.2	603	5.8
RBO23-02	830	1667	0.5	0.0669	0.0015	0.9007	0.0192	0.098	0.001	835	48.1	652	10.3	603	6.1
RBO23-03	4924	6365	0.8	0.0585	0.0013	0.785	0.0197	0.0973	0.0011	550	48.1	588	10.2	598	6.5
RBO23-04	769	1886	0.4	0.0681	0.0014	0.9019	0.0186	0.096	0.0008	872	43.4	653	9.9	591	4.8
RBO23-05	797	1273	0.6	0.066	0.0015	0.8908	0.0206	0.0977	0.0009	809	46.3	647	11.1	601	5.1
RBO23-06	4926	6154	0.8	0.0613	0.0011	0.827	0.0159	0.0978	0.0009	650	38.9	612	8.8	601	5.5
RBO23-07	2568	4815	0.5	0.0599	0.0011	0.8104	0.0157	0.0979	0.0008	598	38.9	603	8.8	602	4.8
RBO23-08	932	1975	0.5	0.0622	0.0013	0.8341	0.0181	0.0971	0.0009	683	46.3	616	10	598	5.2
RBO23-09	605	1317	0.5	0.0631	0.0013	0.8556	0.0176	0.0984	0.001	722	11	628	9.6	605	5.8
RBO23-10	2952	4452	0.7	0.0602	0.0013	0.8057	0.0191	0.0967	0.0009	613	46.3	600	10.7	595	5.1
RBO23-16	953	1985	0.5	0.0676	0.0013	0.9157	0.0158	0.0986	0.0012	855	38.9	660	8.4	606	7.3
RBO23-18	755	484	0.9	0.0606	0.0017	0.8137	0.023	0.0972	0.001	633	59.2	605	12.9	598	5.7
RBO23-19	2605	4758	0.5	0.061	0.0009	0.8288	0.0133	0.0983	0.0008	639	31.5	613	7.4	604	4.9
RBO23-20	2231	2592	0.9	0.0627	0.0001	0.8511	0.014	0.0983	0.0008	698	33.3	625	7.7	604	4.7
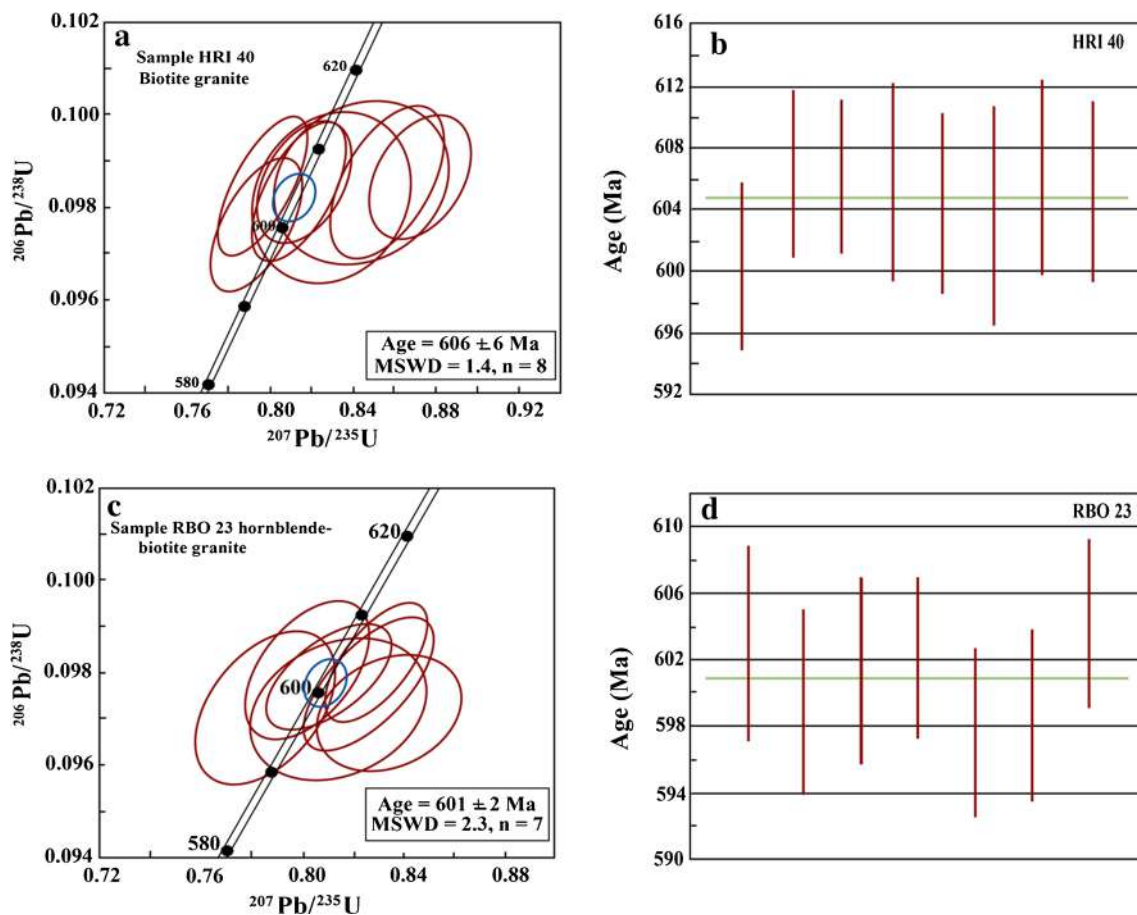
Fig. 8 **a**, **b** Zircon U-Pb concordia plots for the sheared alkaline biotite granites granite of Figuil. **c**, **d** Weighted average zircon U-Pb ages of the sheared alkaline hornblende-biotite granite of Figuil

Feldspar porphyroclasts are often anastomosed by recrystallized quartz and fine fragments of feldspar, quartz, and biotite; at places, these aggregates display shear sense (Fig. 9).

Shear sense indicators

Sigmoid fish A few feldspar crystals show sigmoid fish (Fig. 9). Sometimes, sigmoid fish is also observed with titanites and micas. A typical example is classic feldspar mantle clasts with well-developed recrystallized trials of biotite and quartz mixed with fine grains (Fig. 9b, c). These mineral fish resemble morphologically with Fig. 3a and grain 2 in Figs. 3d and 6a of Mukherjee (2011). They also resemble alpha-type porphyroclast system of Simpson (1986), Passchier and Simpson (1986), and Blenkinsop and Treloar (1995).

Lenticular fish Lenticular fish are commonly observed in quartz and feldspar porphyroclasts (Fig. 10a–d) or in their aggregates. Crystals show shapes that resemble symmetric and asymmetric in augen-gneisses described in Mukherjee (2017). Sometimes, the long axes of the lenticles make an acute angle with the C-planes (Fig. 10a, b) from which the general shear sense can be deduced.

Porphyroclast system It is characterized by porphyroclasts usually of feldspar or quartz, mantles, and mica tails, if base on Passchier and Simpson (1986) classification. Sometimes, the tails show stair stepping on both sides deviating from a horizontal reference line along the center of the porphyroclasts parallel to the planar part of the tail (Fig. 9). Also, some crystals display double mica tails on either sides and are classified as complex types Passchier and Simpson (1986). A few of the porphyroclasts show well-developed stair stepping tails, which extent to the mylonitic foliations (Fig. 9). This clast-tail system probably indicates that the rate of recrystallization at the tail were higher than clast rotation rates (e.g., Ishii et al. 2007; Menegon et al. 2017). Both dextral and sinistral shear senses were deduced from the stepping up direction defined by the median line (Fig. 9a–c). Feldspar porphyroclasts and dynamic

Fig. 9 Photomicrographs under CPL: **a–c** elegant sigmoid K-feldspars fish indicating sinistral shear, **b** core-mantle K-feldspars anastomose by mica with dextral shear, **c** classic feldspar mantle clast with recrystallized trails of biotite and quartz indicating dextral shear, **d** core-mantle K-feldspar
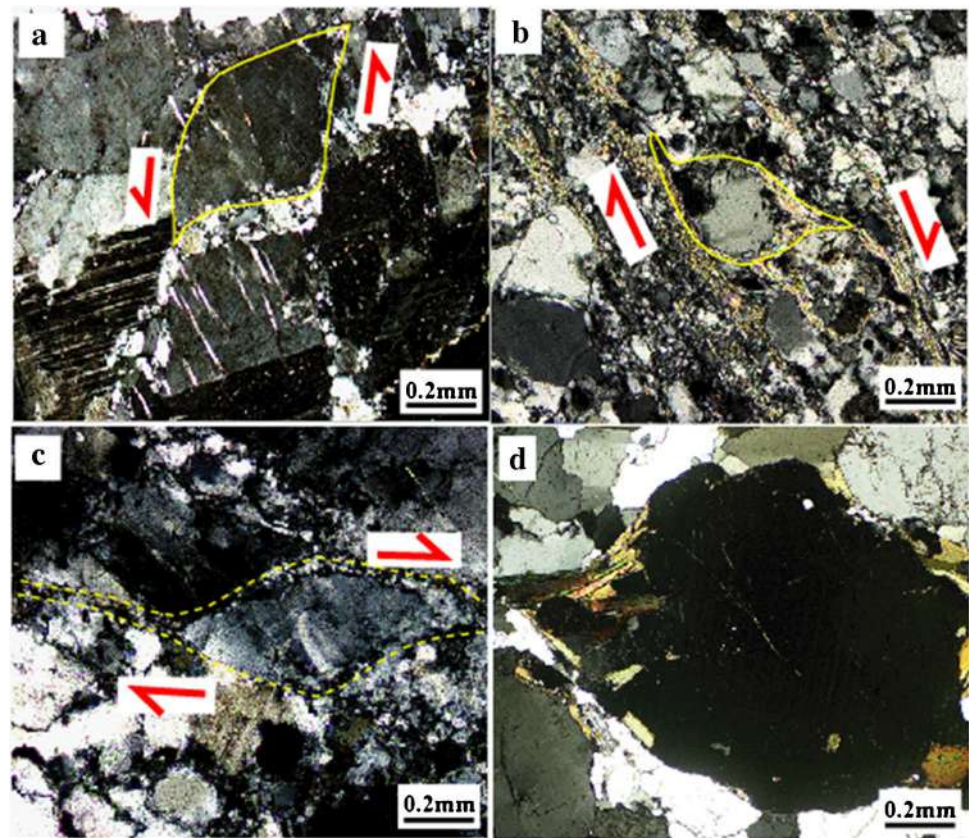
recrystallized aggregates of feldspar and quartz define a mylonitic foliation (S) (Fig. 10a, b). This mylonitic foliation is enclosed by C-planes and together defined σ_b-type C/S fabrics (Fig. 10a–e), which are oblique to the C-planes from which a dextral shear sense is deduced (Fig. 10a, b).

Core-mantle porphyroclasts within the C/S fabrics in the mylonite display shear fractures (microfaults) (Fig. 10i). The microfaults show oblique orientation with the C-planes that enclosed the clast (domino-structure) (Fig. 10g, h). Both dextral and sinistral shear senses are deduced from the displaced fragments in the clast within the mylonite (Fig. 10g, h). It, therefore, demonstrates that the GSSZ probably experienced complicated shear events.

Extensional features

Pull-aparts and boudins Feldspar porphyroclasts are dragged out by intracrystalline deformation to boudins (gash boudin) (Mukherjee 2014) (Fig. 11). A few "boudinage veins" contain poorly oriented fragments of crushed adjacent minerals, late crystallized products, and recrystallized grains of biotite, quartz, chlorite, and quartz ribbons (Fig. 11a). As per Vernon (2011), it indicates late phase (sub)magmatic deformation crystallization. Zone A (low-strain zone) boudins are typical microfractures consisting of refilled fragments recrystallized to neocrystallized

aggregates (Fig. 11a). Some fragments within this microfault at times are sheared in similar direction; however, we did not consider them as capable to determine the shear sense (Fig. 11a). Zone B (high-strain zone) boudins consist of equand to equigranular aggregates dominantly of plagioclase and K-feldspar (Fig. 11b, e) bounded by C-planes. A sinistral orientation of some minerals (e.g., plagioclase) within the aggregate with respect to C-planes is use to deduce the shear sense (Fig. 11e).

V-pull-apart microstructures Feldspar laths show asymmetric pull-apart microstructural features by "V"-shaped gap separating fragments (Hippertt 1993). Biotite, titanite, and feldspar of the studied sections show similar features characterized by breakage and rotation of one fragment with respect to the other (Fig. 10d). At times, crystals are separated by curve "V" gaps filled by recrystallized quartz (Fig. 10d). Titanites are dragged and separated by type-1 pull-apart fractures (Fig. 11e).

Discussions

Pluton emplacement and age

Within the Pan-African mobile belt of Cameroon, the studied syn-kinematic plutons have been associated with large shear zones and thrusts and are characterized as the main tectonic
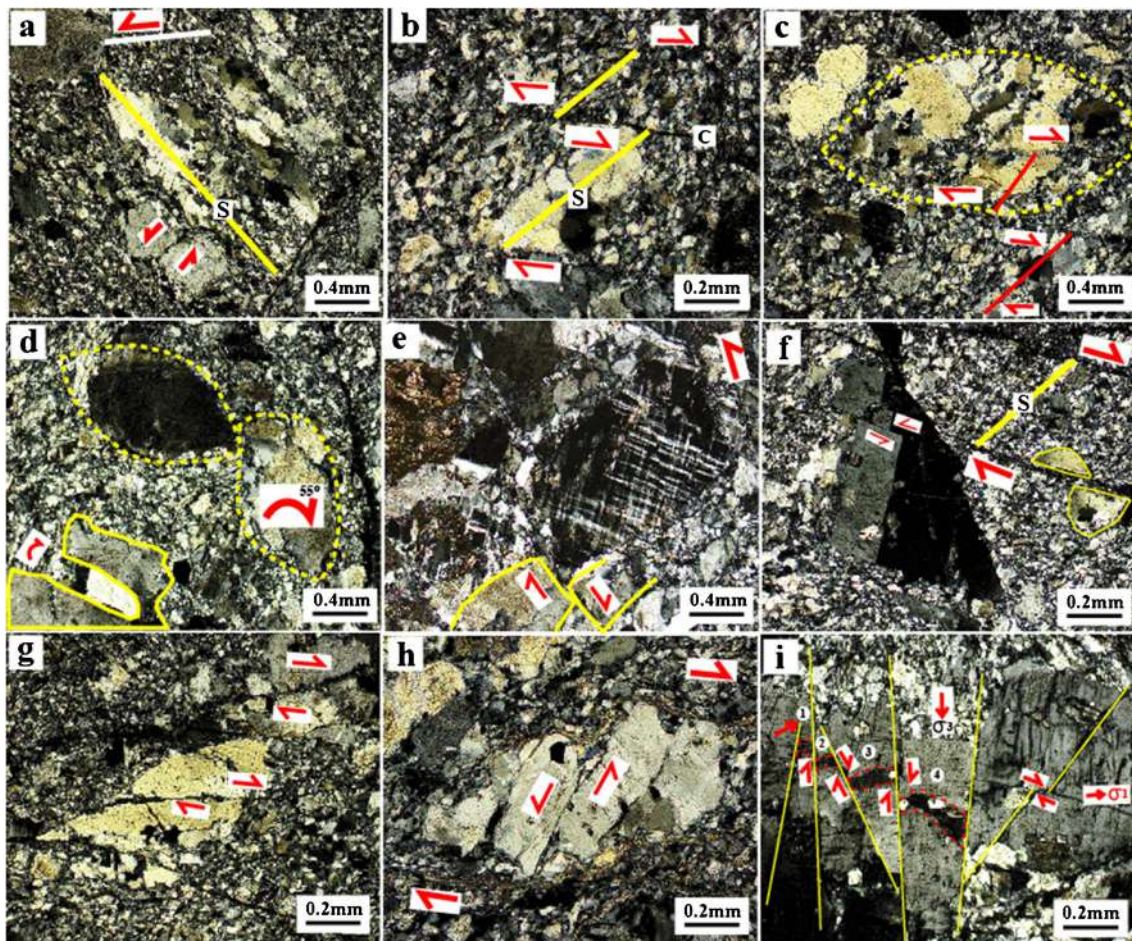
Fig. 10 Photomicrographs under CPL: **a** partially recrystallized quartz obliquely oriented to C-planes; **b–e** lenticular K-feldspar porphyroclasts bound by discrete microshears; **f** bookshelf structure of feldspar porphyroclast, a hat-shaped yellow grain indicating antithetic sense of shear (Mukherjee S, 2012); **g** crosscutting microshearing or shear band type of feldspar porphyroclast showing dextral and sinistral shear; **h** fragmented lenticular feldspars porphyroclast of domino-type indicating dextral and sinistral shear with V-pull-apart; **i** multi-layer strike-slip faults (microfaulting) in feldspars porphyroclast

features. The sheared Heri and Ribao plutons are located near the studied N-S oriented shear zone that may suggest their strong association. The formation of such shear zones within the mobile belt has been linked to collision evolution between the West African craton (WAC), the Sahara Meta-craton (SM), and the Sao Francisco-Congo craton (SFCC). Based on structural evolution history (e.g., Ngako et al. 2008; Dawaï et al. 2013), the studied sheared plutons at Figuil were emplaced in a transpressive setting shortly after a regional thickening event < 620 Ma. A similar environment of formation was previously reported for the nearby syenitic pluton of Guider (Dawaï et al. 2013), for the granitic complex of Batie (Njiekak et al. 2008), and the granitic complex of Bafoussam (Djouka Fonkwe et al. 2008). Magmatism in the northern Cameroon domain commenced during or shortly after the assemblage of these adjacent domains < 612 Ma (Penaye

et al. 2006). It is possible that the collision events caused a sort of increased temperature and strain localization, which led to the initiation of a rheologically weaken mechanical zone through which magma flows to the near surface levels. The obtained U-Pb zircon ages of the studied sheared plutons from 601 ± 2 to 606 ± 6 Ma (Fig. 8) are consistent with the syn-collisional granite within the Babouri-Figuil Magmatic Complex (Basua 2021; Basua et al. 2022). Based on previous studies, ages < 612 Ma marked the final collision phase (Penaye et al. 2006; Basua 2021; Basua et al. 2022). Overall, the magma for these granites was generated probably during the collision evolution between the northern Cameroon domain and the southern Chad domain. Therefore, the initiation and reactivation of the Guider Sorawel shear zone played essential role for the emplacement and post shearing of the studied massifs (Basua 2021).

Fig. 11 Photomicrographs under CPL: **a**–**f** pinch and swells in minerals and mineral aggregates (mica, titanite, feldspars, and quartz) and microveins, indicating sinistral and dextral shear senses
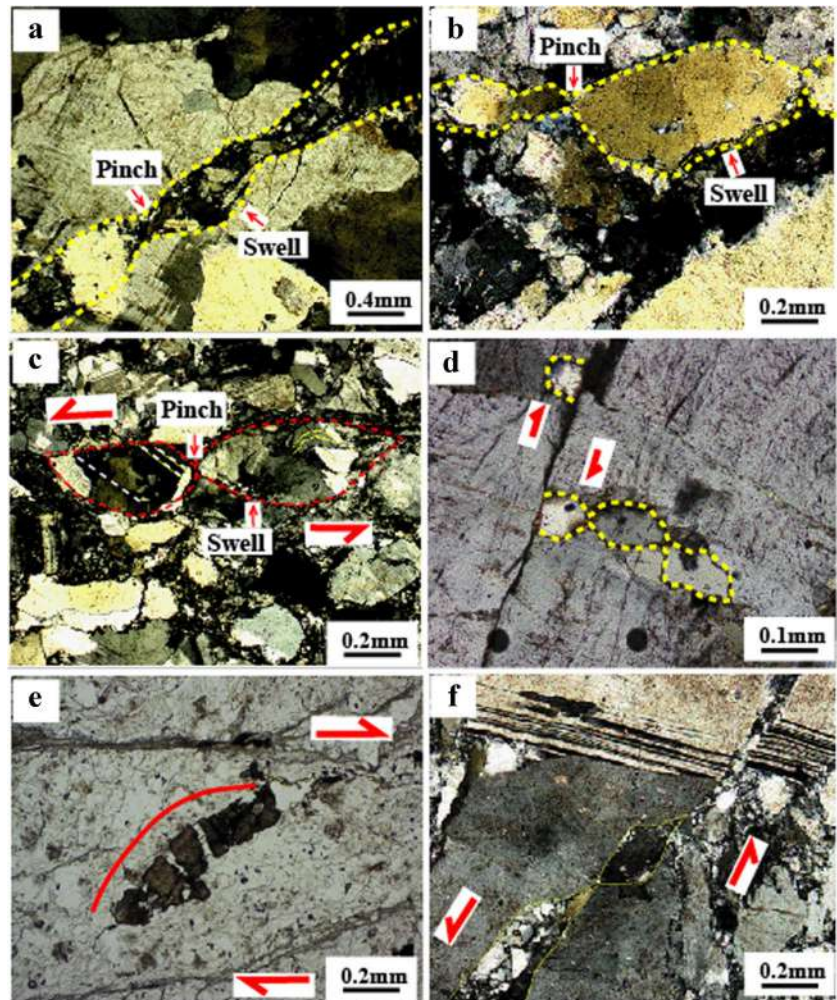
Significance of microstructures within the GSSZ

The studied microstructures deduced that the Guider-Sorawel shear zone (GSSZ) is a ductile tectonic deformation (Figs. 2, 9, 10, and 11). Similar ductile shear zones have been studied across Cameroon (Njome et al. 2003; Sigue et al. 2023; Yomeun et al. 2023).

Quartz crystals that show polycrystalline aggregate ribbons with grain boundary migration indicate medium to high temperature plastic deformation conditions (Passchier and Trouw 2005; Hansen et al. 2013; Cavalcante et al. 2018; Dong et al. 2019) (Fig. 10). Moreover, the deformed quartz grains with dominant slip system indicate conditions sensitive to temperatures (Stipp et al. 2002). For instance, prism <a> slip frequently occurs in high-grade metamorphic rocks (Cao et al. 2013), whereas basal <a> slip is mostly associated with low-grade or overprinted metamorphic rocks (Toy et al. 2008; Cao et al. 2013; Chen et al. 2018). Some quartz crystals in the GSSZ show low-angle rotation axis and C-axis patterns suggesting dominated high-temperature zones (Chen et al. 2018) (Fig. 6c).

In short, the quartz grains within the GS shear zone have suffered a sort of medium to high temperatures (> 400 to ~ 700 °C) dislocation creep deformation (Dong et al. 2019; Fig. 12).

In zone B, the domino microfaulting in some porphyroclasts by either subsequent microshear indicate increase strain zone (Fig. 10e, f). The intense grain-size reduction in the high-strain zone "B" is proportionate to high-grade temperature conditions relative to diffusion creep deformation mechanism (e.g., Miranda et al. 2016; Dong et al. 2019). In the low-strain zone, the low-angle misorientation angles of some plagioclase and K-feldspar suggest the development of intragranular deformation. It, therefore, demonstrates that dislocation creep is the principal mechanism of feldspar deformation within the GSSZ (e.g., Menegon et al. 2017). Based on previous studies, feldspar deformation mechanism can be linked to activation slip system of (010) <101> or <100> (e.g., Ishii et al. 2007; Menegon et al. 2017).

In zone A (low-strain zone), the random distribution of feldspar grains may not be described by dislocation creep and myrmekites induced by dynamic recrystallization, but

indicate a complicated mechanism during feldspar deformation. Previous studies suggest dissolution-precipitation creep (Menegon et al. 2008; Dong et al. 2019) and grain boundary diffusion (Ishii et al. 2007). In zone B (high-strain zone), the fine-grained feldspars show equant to slightly elongated shape, rare low-angle grain boundaries, and uncorrelated misorientation distribution. Sometimes, these grains are aligned parallel to the displacement direction indicating grain boundary sliding (e.g., Kilian et al. 2011; Mansard et al. 2018). According to previous studies, grain boundary sliding (GBS) deformation mechanism could result from the weakening of phase mixing and grain-size reduction (e.g., Miranda et al. 2016; Mansard et al. 2018).

Shear sense indicators

Figures 2 (mega), Figs. 3, 4, and 5 (macro), and Figs. 6, 9, and 10 (microstructures) are used to describe the orientation of the Guider-Sorawel shear zone. Figure 2 indicates a mega-scale sinistral displacement of the western edge of the Heri massif probably after the complete crystallization of the magma. It, therefore, confirms that the sinistral movement is a post-dextral reactivation of the GSSZ and support that the observed microstructures were developed at the

sub-magmatic phase. On the outcrop scale, the studied granites revealed several generations of veins (Fig. 5a, b), shear bands (Fig. 4d–f), and faults (Fig. 5d) with crosscutting patterns, which resemble those of the host metamorphic rocks (Fig. 3a, b). These shear bands indicate both dextral and sinistral shear sense, respectively (Fig. 3a–d). A mafic xenolith with long axis parallel to mineral lineations of the host metamorphic rock demonstrates sinistral shear (Fig. 5c). The displacement gaps (sinistral) of the mafic xenolith and a second-generation fault on the granite are similar ~ 15 cm suggesting that the late sinistral movement in both rocks was synchronous (Fig. 5c, d).

Kinematic indicators revealed at least two ductile shear sense (dextral and sinistral) (Figs. 9, 10, and 11). Similar studies have been reported elsewhere in Cameroon (e.g., Efon Awoum et al. 2020; Dawaï et al. 2017; Sigue et al. 2023). Our results indicate crosscut relation (Fig. 5d), which for the purpose of this study are classify as early and late shears. It confirms separate deformation phases since previous studies have indicated that the absence of crosscut relation in multiple-stage deformation could suggest synchronous event (Langille et al. 2010; Little et al. 2013). The early shear fabrics, e.g., mylonitic foliations (Fig. 10a–d), were crosscut by late mylonitic C-planes (Fig. 10a–d). The

Fig. 12 Summary of the thermal ranges of mineral deformation mechanism of sub-magmatic to solid-state microstructures of granites of the Figuil-Sorawel shear zone (modified from Fazio et al. 2020, temperature ranges after, Passchier and Trouw 2005). BLG, bulging recrystallization; SGR, subgrain rotation recrystallization; GBM, grain boundary migration recrystallization
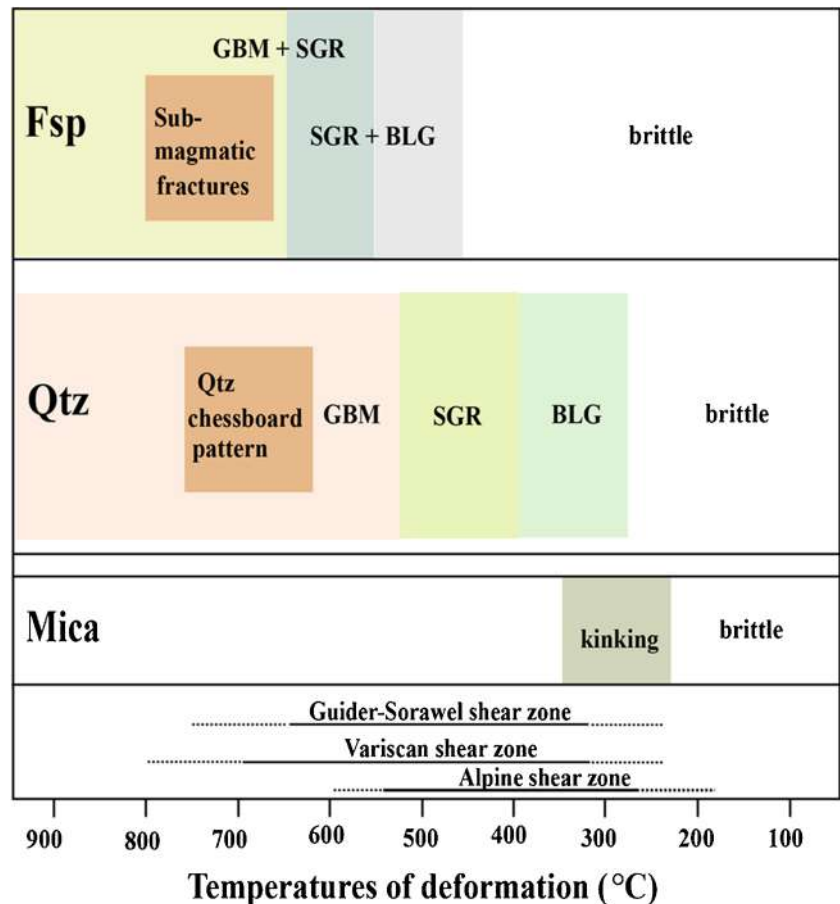
majority of micas fish, asymmetric folds, quartz lattice preferred orientation, and micro-boudins are sub-magmatic features. The micro-dextral shear is consistent with the dextral shear of asymmetric B_2 boudins of quartz-feldspar and tonalitic injections observed in gneisses outcrops (Fig. 3e, f).

Microstructural evolution study of the Etam shear zone (SW-Cameroon) also revealed early dextral and late sinistral shear movements suggesting reactivation event (Sigue et al. 2023). Similar double shear events with earlier dextral and late sinistral movements have been reported by Ntieche et al. (2017) and Efon Awoum et al. (2020) from sheared granitoids in west Cameroon. However, studies conducted by Dawaï et al. (2013) suggested that both dextral and sinistral shear movements maybe synchronous. The combined results, therefore, suggest a complex kinematic deformation evolution within the Pan-African mobile belt of Cameroon.

Formation conditions and processes of the GSSZ

Structural studies of the GSSZ reveal ductile deformation processes. Formation of this SZ might be related to Pan-African collision of tectonic terrains. Structural features suggest shallow-deep crustal levels. The progressive plastic deformation behavior of the principal minerals (quartz, plagioclase, and K-feldspar) was in response to the intense ductile deformation records either from sub-magmatic or to solid state. Based on the obtained results in this work coupled with the structural deformation history in Ngako et al. (2008), it suggests that the studied shear zone either experienced medium-high temperatures deformation conditions at least amphibolites facies during the dominant ductile shearing (Fig. 12). The similar microstructural features, e.g., mylonitic foliations, lineations, and boudins in both the granite and host rocks demonstrate identical syn-kinematic metamorphic structures. It confirms that the shearing of these granites presumably occurred simultaneously during metamorphic deformation of the basement rock. Biotite estimated temperatures of the studied granites range between 647 and 695 °C at < 5 kb (Basua et al. 2022). Similar temperature conditions are revealed by microstructures of the studied sheared granites at shallow crustal levels (Fig. 12).

Shear zones are usually localized in rheologically weaken mechanical zones (e.g., Fossen and Cavalcante 2017; Liu 2017; Pennacchioni and Mancktelow 2018). Besides temperatures and pressure, these zones of weakness can be activated by mineralogy, strain rate, microstructure, texture, and fluid during strain localization (e.g., Liu 2017; Pennacchioni and Mancktelow 2018). Localization may occur in external inhomogeneity zones such as in precursor fractures or joints (Menegon and Pennacchioni 2009). The combine field and microstructures in this work reveal complex shearing events. For instance, the high-temperature deformation conditions confirm that the initiation of the Guider-Sorawel shear zone

might have occurred at depth, where weakening mechanisms such as temperature-controlled rheology can play significant role in localizing new shear zones (Menegon and Pennacchioni 2009). A progressive shear event probably occurred at shallow crustal level during reactivation of a precursor fault or joint.

Tectonic evolution model

Figure 13 presents a simple two-stage 3D tectonic model to summarize the transcurrent tectonic evolution in Figuil. The presence of tight and upright folds, which opens toward the north or south (fold axes and mineral lineations N-S to NE-SW), indicates WNW-ESE to W-E compression in a transpression region during the collision < 612 Ma between the north-Cameroon and Mayo-Kebbi domains (Penaye et al. 2006; Ngako et al. 2008). According to Toteu et al. (2001), the northwest Cameroon domain experiences relative changed of its principal stress direction from the NW to N (< 612 Ma) and back to NW (< 590 Ma). Our results, based on mega-, meso-, and microscale, reveal early dextral and late sinistral shears consistent with the change of the principal stress direction. This strongly confirms a possible fault reactivation induced by the change of the principal stress direction. We suggest that the start of collision < 612 Ma enhanced by the clockwise rotation of the principal stress direction (NW to N) invoked early general shear with dextral simple shear component. Subsequent collisions < 590 Ma followed by anticlockwise rotation (N to NW) induce sinistral reactivation of the simple shear.

Conclusions

1. Similar dates of 606 ± 6 and 601 ± 2 Ma of the sheared biotite granite and hornblende-biotite granite from the Heri and Ribao massifs, respectively, are interpreted as their syn- to late-collisional emplacement. These ages are contemporaneous to E-W transpression (~ 612 Ma) after crustal thickening and thrusting events in Cameroon, which lasted 620 Ma.
2. Structural data indicate non-coaxial double shear and are classified based on crosscutting relation as early and late. The early event could be dated between 600 and 593 Ma and display dextral shear. The late shear is sinistral and could be dated at < 590 Ma.
3. The double shear is possible by post-reactivation of the N-S trending Guider-Sorawel fault during the change of the maximum stress direction from N-S (~ 600 Ma) to NW-SE (< 590 Ma) in a transpressive regime during and after the emplacement of the plutons.
4. We suggest that the studied unknown N-S trending Guider-Sorawel shear zone could represent the NE
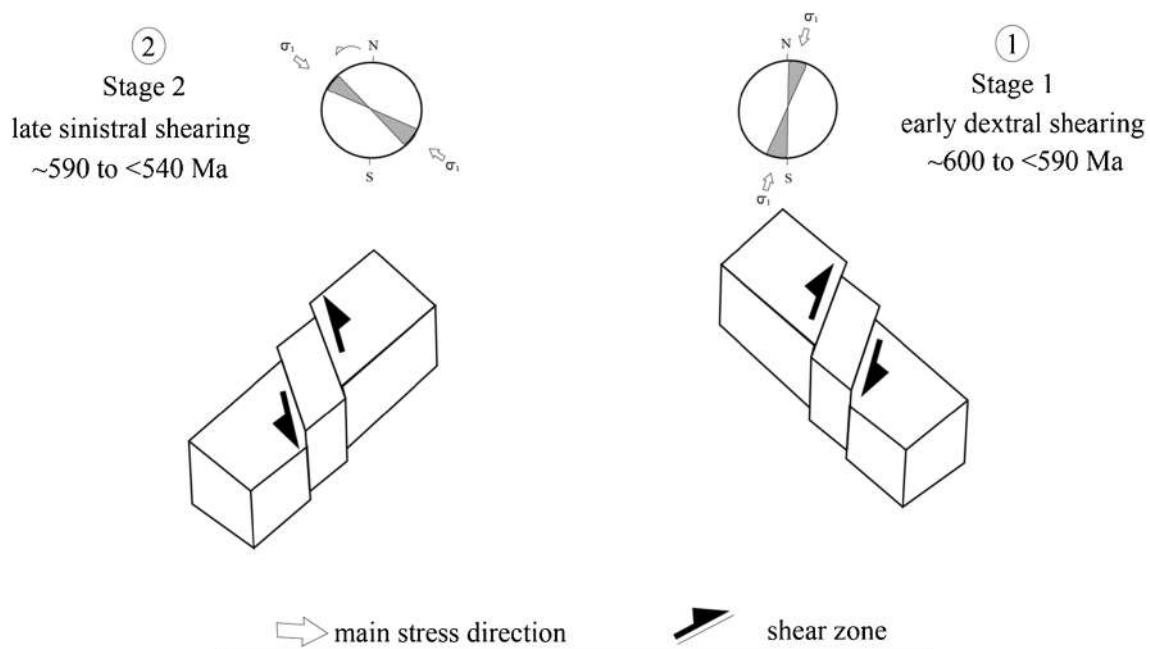
Fig. 13 Two stages simplified 3D tectonic model characterizing the N-S Guider-Sorawel shear zone in a transpression tectonic regime in Figuil: (a) stage 1, early dextral shear movement ~ 600 to < 590 Ma and (b) stage 2 late sinistral shear movement ~ 590 to < 540 Ma

extension of the sinistral Balche shear zone well exposed in the Poli Group of the NCD. Also, it could indicate a terrane boundary between the Ribao, Heri (~ 600 Ma) and Lombel, Badesi (> 570 Ma) massifs.

Declarations

Conflict of interest The authors declare no competing interests.

References

Abdelsalam MG, Liégeois J-P, Stern RJ (2002) The Saharan Metacraton. Journal of African Earth Sciences 34:119–136

Archanjo CJ, Hollanda MHBM, Rodrigues SW, Brito Neves BB, Armstrong R (2008) Fabrics of pre- and syntectonic granite plutons and chronology of shear zones in the Eastern Borborema Province, NE Brazil. Journal of Structural Geology 30:310–326

Basua AAE (2021) Geochronology and petrogenesis of the Pan-African A-type granitoids from the Babouri-Figuil Complex, NW Cameroon domain: implication for the tectonic evolution of the central Africa. Ph.D. Thesis. China University of Geosciences, Wuhan, p 260

Basua AAE, Ma C, Nguo KS, Wang L-X, Lentz DR, Mukherjee S, Nformidah-Ndah SS, Yomeun BS (2022) Petrogenesis and tectonic setting of A-type granites in the Babouri-Figuil Magmatic Complex (North Cameroon): constraints from whole rock geochemistry, zircon UPb geochronology and Sr-Nd-Hfisotopes. Lithos 414:106618

Blenkinsop TG, Treloar PJ (1995) Geometry, classification and kinematics of SC and SC′ fabrics in the Mushandike area. Zimbabwe, Journal of Structural Geology 17(3):397–408

Cao S, Neubauer F, Bernroider M, Liu J (2013) The lateral boundary of a metamorphic core complex: the Moutsounas shear zone on Naxos, Cyclades, Greece. J. Struct. Geol. 54:103–128

Cavalcante C, Lagoeiro L, Fossen H, Egydio-Silva M, Morales LFG, Ferreira F, Conte T (2018) Temperature constraints on microfabric patterns in quartzofeldsphatic mylonites, Ribeira belt (SE Brazil). J. Struct. Geol. 115:243–262

Chen K, Scales M, Kyriakides S (2018) Ductile failure under combined tension and shear. Conference Series, Journal of Physics, p 1063

Coleman DS, Bartley JM, Glazner AF, Law RD (2005). Incremental assembly and emplacement of Mesozoic plutons in the Sierra Nevada and White and Ranges I, California. Geological Society of America Field Forum Field Trip Guide (Rethinking the assembly and evolution of plutons: field tests and perspectives, 7–14 October, 2005.

Dawaï D, Bouchez J-L, Paquette J-L, Tchameni R (2013) The Pan-African quartz-syenite of Guider (north-Cameroon): magnetic fabric and U–Pb dating of a late-orogenic emplacement. Precambrian Research 236:132–144

Dawaï D, Tchameni R, Bascou J, Awe Wangmene S, Tchunte PM, Bouchez JL (2017) Microstructures and magnetic fabrics of the Ngaoundéré granite pluton (Cameroon): implications to the late-Pan-African evolution of central Cameroon shear zone. J. Afr. Earth Sci. 129:887–8897

Djouka Fonkwe ML, Schulz B, Schussler U, Tchouankoue JP, Nzolang C (2008) Geochemistry of the Bafoussam Pan-African I- and Stype granitoids in western Cameroon. J. Afr. Earth Sci. 50:148–167

Dong Y, Cao S, Cheng X, Liu J, Cao H (2019) Grain-size reduction of feldspar and flow of deformed granites within the Gaoligong shear zone, southwestern Yunnan, China. Sci. China-Earth Sci. 62:1379–1398

Efon Awoum J, Fozing EM, Kwekam M, Tcheumenak Kouemo J, Choumele Kana SC, Achu Megnemo L (2020) Structural characterization of the pan-african ndieki area in the foumban-bankim shear zone (West Cameroon): Constraints from field observations and microstructures. Arabian J Geosci 13:831–847

Fazio E, Fiannacca P, Cirrincione R (2020) Submagmatic to solid-state deformation microstructures recorded in cooling granitoids during exhumation of lateVariscan crust in north-eastern Sicily. Geosciences 10:1–29. https://doi.org/10.3390/geosciences10080311

Fossen H, Cavalcante GCG (2017) Shear zones–a review. Earth-Sci. Rev. 171:434–455

Günther D, Heinrich A (1999) Enhanced sensitivity in laser ablation-ICP mass spectrometry uing helium-argon mixtures as aerosol carrier. Journal of Analytical Atomic Spectrometry 14(9):1363–1368

Hansen LN, Cheadle MJ, John BE, Swapp SM, Dick HJB, Tucholke BE, Tivey MA (2013) Mylonitic deformation at the Kane oceanic core complex: implications for the rheological behavior of oceanic detachment faults. Geochem. Geophys. Geosyst. 14:3085–3108

Hippertt JFM (1993) 'V'-pull-apart microstructures: a new shear-sense indicator. Journal of Structural Geology 15(12):1393–1403

Hu Z (2014) "Wave" signal-smoothing and mercury-removing device for laser ablation quadrupole and multiple collector ICPMS analysis: application to lead isotope analysis. Analytical chemistry 87(2):1152–1157

Ishii K, Kanagawa K, Shigematsu N, Okudaira T (2007) High ductility of K-feldspar and development of granitic banded ultramylonite in the Ryoke metamorphic belt, SW Japan. J. Struct. Geol. 29:1083–1098

Jackson SE, Pearson NJ, Griffin WL, Belousova EA (2004) The application of laser ablation-inductively coupled plasma-mass spectrometry to in situ U–Pb zircon geochronology. Chemical Geology 211(1):47–69

Kilian R, Heilbronner R, Stünitz H (2011) Quartz grain size reduction in a granitoid rock and the transition from dislocation to diffusion creep. J. Struct. Geol. 33:1265–1284

Langille J, Lee J, Hacker B, Seward G (2010) Middle crustal ductile deformation patterns in southern Tibet: insights from vorticity studies in Mabja Dome. Journal of Structural Geology 32(1):70–85

Little TA, Hacker BR, Brownlee SJ, Seward G (2013) Microstructures and quartz lattice-preferred orientations in the eclogite bearing migmatitic gneisses of the D'Entrecasteaux Islands, Papua New Guinea. Geochem. Geophys. 14:2030–2062

Liu JL (2017) Strain localization and strain weakening in the continental middle crust. Acta Petrol. Sin. 33:1653–1666

Liu YS, Gao SHZ, Gao CG, Zong KQ, Wang DB (2010) Continental and oceanic crust recycled-induced melt-peridotite interactions in the Trans-North China Orogen: U-Pb dating, Hf isotope and trace elements in zircons of mantle xenoliths. J Petrol 51:537–571

Liu YS, Hu ZC, Gao S, Gunther D, Xu J, Gao CG, Chen HH (2008) In situ analysis of major and trace element of anhydrous, minerals by LA-ICP-MS without applying an internal standard. Chem Geol 257:34–43

Ludwig KR (2003) Isoplot 3.00: a geochronological toolkit for Microsoft Excel, Berkeley Geochronology Center Special. Publication 4:70

Luo T (2018) Reassessment of the influence of carrier gases He and Ar on signal intensities in 193nm excimer LA-ICP-MS analysis. Journal of Analytical Atomic Spectrometry 33(10):1655–1663

Mansard N, Raimbourg H, Augier R, Précigout J, Le Breton N (2018) Large-scale strain localization induced by phase nucleation in mid-crustal granitoids of the south Armorican massif. Tectonophysics 745:46–65

Menegon L, Pennacchioni G (2009) Local shear zone pattern and bulk deformation in the Gran Paradiso metagranite (NW Italian Alps). Int. J. Earth Sci. 99:1805–1825

Menegon L, Pennacchioni G, Malaspina N, Harris K, Wood E (2017) Earthquakes as precursors of ductile shear zones in the dry and strong lower crust. Geochem. Geophys. Geosyst. 18:4356–4374

Menegon L, Pennacchioni G, Spiess R (2008) Dissolution-precipitation creep of K-feldspar in mid-crustal granite mylonites. J. Struct. Geol. 30:565–579

Miranda EA, Hirth G, John BE (2016) Microstructural evidence for the transition from dislocation creep to dislocation-accommodated grain boundary sliding in naturally deformed plagioclase. J. Struct. Geol. 92:30–45

Mukherjee S (2011) Mineral fish: their morphological classification, usefulness as shear sense indicators and genesis. International Journal of Earth Sciences 100(6):1303–1314

Mukherjee S (2012) Simple shear is not so simple! Kinematics of Newtonian viscous simple shear zones. Geol Mag 149:819–826

Mukherjee S (2013) Deformation microstructures in rocks. Springer Geochemistry/Mineralogy, Berlin, p 111

Mukherjee S (2014) Review of flanking structures in meso- and micro-scales. Geological Magazine 151:957–974

Mukherjee S (2017) Review on symmetric structures in ductile shear zones. International Journal of Earth Sciences 106:1453–1468

Mukherjee S, Koyi HA (2010) Higher Himalayan shear zone, Zanskar Indian Himalaya: microstructural studies and extrusion mechanism by a combination of simple shear and channel flow. International Journal of Earth Sciences 99(5):1083–1110

Mumbfu EM, Nforba MT, Suh CE (2014) Geochemical dispersion of gold in stream sediments in the Paleoproterozoic Nyong Series, Southern Cameroon. Science Research 2(6):155–165

Ngako V, Affaton P, Njonfang E (2008) Pan-African tectonics in northwestern Cameroon: implication for the history of western Gondwana. Gondwana Research 14(3):509–522

Ngako V, Njonfang E (2011) Plates amalgamation and plate destruction, the Western Gondwana history. Tectonics, INTECH London, p 34

Njiekak G, Dorr W, Tchouankoue JP, Zulauf G (2008) U-Pb zircon and micro-fabric data of (meta) granitoids of western Cameroon: constraints on the timing of pluton emplacement and deformation in the Pan-African belt of central Africa. Lithos 102:460–477

Njome MS, Suh CE, Ghogomu RT (2003) A microstructural approach to interpreting the structural setting of the Tombel graben, south western Cameroon. Geo Acta **2**:181–200

Njonfang E, Ngako V, Moreau C, Affaton P, Diot H (2008) Restraining bends in high temperature shear zones: the "central Cameroon shear zone", Central Africa. J Afr Earth Sci 52(1-2):9–20

Nsengimana S, Kumar GRS (2019) Microstructures investigation on economic minerals and their associated rocks occurred in Usillampatti Taluk, Madurai district, South India

Ntieche B, Mohan MR, Amidou M (2017) Granitoids of the Magba shear zone, west Cameroon, Central Africa: evidences for emplacement under transpressive tectonic regime. J. Geo. Soc. India 89(1):33–46. https://doi.org/10.1007/s12594-017-0556-4

Nzenti JP, Kapajika B, Worner G, Lubala TR (2006) Synkinematic emplacement of granitoids in a Pan-African shear zone in central Cameroon. J. Afr. Earth Sci. 45:74–86

Passchier CW, Simpson C (1986) Porphyroclast system as kinematic indicators. Journal of Structural Geology 8:831–844

Passchier CW, Trouw RAJ (2005) Microtectonics. Springer, Berlin/Heidelberg, Germany ISBN 3-540-64003-7

Penaye J, Kröner A, Toteu SF, Van Schmus WR, Doumnang JC (2006) Evolution of the Mayo Kebbi region as revealed by zircon dating: an early (ca. 740 Ma) Pan-African magmatic arc in southwestern Chad. Journal of African Earth Sciences 44(4-5):530–542

Pennacchioni G, Mancktelow NS (2018) Small-scale ductile shear zones: neither extending, nor thickening, nor narrowing. Earth-Sci. Rev. 184:1–12

Punturo R, Cirrincione R, Fazio E, Fiannacca P, Kern H, Mengel K, Ortolano G, Pezzino A (2014) Microstructural, compositional and petrophysical properties of mylonitic granodiorites from an extensional shear zone (Rhodope Core complex, Greece). Geol. Mag. 151:1051–1071

Radlinski AP, Hinde AL, Rauch H, Hainbuchner M, Baron M, Mastalerz M, Ioannidis M, Thiyagarajan P (2005) The microstructure of rocks and small-angle and ultra-small-angle neutron scattering: the coming of age of a new technique. Geophysical Research Abstracts 7:03865 SRef-ID: 1607-7962/gra/EGU05-A-03865

Shellnutt JG, Lee TY, Yang CC, Hu ST, Wu JC, Wang KL, Lo CH (2015) Late Permian mafic rocks identified within the Doba basin of southern Chad and their relationship to the boundary of the Saharan Metacraton. Geological Magazine 152(6):1073–1084

Sigue C, Cheo ES, Ndema JLM (2023) Structural and microstructural evolution of Etam shear zone in the Central Africa Fold Belt, SW-Cameroon: implication of hydrothermal syn-tectonic quartz vein formation. Arab J Geosci 16:341

Simpson C (1986) Determination of movement sense in mylonites. Journal of Geological Education 34(4):246–261

Stipp M, Stünitz H, Heilbronner R, Schmid SM (2002) The eastern Tonale fault zone: a "natural laboratory" for crystal plastic deformation of quartz over a temperature range from 250 to 700 _C. J. Struct. Geol. 24:1861–1884

Tagne-Kamga G, Mercier E, Rossy M, Nsifa Nkonguin E (1999) Synkinematic emplacement of the Pan-African Ngondo igneous complex (West Cameroon, central Africa). J. Afr. Earth Sci. 28:675–691

Toteu SF, Penaye J, Djomani YP (2004) Geodynamic evolution of the Pan-African belt in central Africa with special reference to Cameroon. Canadian Journal of Earth Sciences 41(1):73–85

Toteu SF, Schmus V, Penaye J, Michard A (2001) New U-Pb and Sm-Nd data from north-Central Cameroon and its bearing on the pre-Pan-African history of Central Africa. Precambrian Res 108:45–73

Toy VG, Prior DJ, Norris RJ (2008) Quartz fabrics in the Alpine Fault mylonites: influence of pre-existing preferred orientations on fabric development during progressive uplift. J. Struct. Geol. 30:602–621

Van Schmus W, Oliveira E, Da Silva FA, Toteu S, Penaye J, Guimarães I (2008) Proterozoic links between the Borborema province, NE Brazil, and the Central African fold belt. Geological Society, London, Special Publications 294(1):69–99

Vernon R (2011) Microstructures of melt-bearing regional metamorphic rocks. Geological Society of America Memoirs 207:1–11

Wiedenbeck M (1995) Three natural zircon standards for U-Th-Pb, Lu-Hf, trace element 1096 and REE analysis. Geostandards Newsletter 19(1):1–23

Yomeun BS, Wang W, Tchoankoue JP, Kamami MSK, Azeuda KNI, Basua AAE (2023) Microstructural constraints on the Pan-African syn-kinematic magmatism in the Adamawa-Yade domain, Cameroon. Arab J Geosci 16:567

Zong K, Klemd R, Yuan Y, He Z, Guo J, Shi X, Liu Y, Hu Z, Zhang Z (2017) The assembly of Rodinia: The correlation of early Neoproterozoic (ca. 900 Ma) high-grade metamorphism and continental arc formation in the southern Beishan Orogen, southern Central Asian Orogenic Belt (CAOB). Precambrian Res 290:32–48